ACS APPLIED NANO MATERIALS

www.acsanm.org Article

Shockley–Read–Hall Recombination in Indium Gallium Nitride Nanolayer: A Density Functional Theory Study

Kisang Byun, Arindam Sannyal, Dohee Kim, Sang Ho Jeon, Sung-Chan Jo,* and Joonkyung Jang*

Cite This: *ACS Appl. Nano Mater.* 2026, 9, 9478–9486 Read Online

ACCESS | Metrics & More | Article Recommendations | Supporting Information

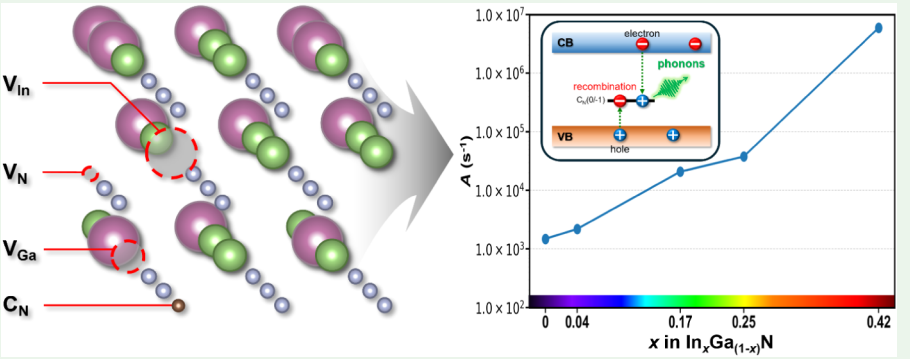

ABSTRACT: Indium gallium nitride (InGaN) is widely used in light-emitting diodes (LEDs) because of its excellent stability and quantum efficiency (QE). By increasing the In concentration, an InGaN LED changes its color from blue to green and red. Currently, InGaN with green-to-red emission suffers from low QE, and its efficiency degradation mechanism is insufficiently understood. Using the density functional theory, we investigated the impact of point defects on the Shockley–Read–Hall (SRH) recombination in the InGaN nanolayer. In particular, we determined defect formation energies, charge transition levels, and carrier capture coefficients for the SRH recombination by systematically varying the In content. It was found that a nitrogen atom substituted by carbon was a dominant deep acceptor whose capture coefficient increased with increasing In concentration.

KEYWORDS: *density functional theory, light emitting diode, Shockley–Read–Hall recombination, capture coefficient, defect formation energy, transition level, indium gallium nitride*

INTRODUCTION

Display technologies are applied to various electronic devices ranging from wearable devices to large-scale displays, and their application scope is continually broadening.[1] In mobile devices, the display consumes the largest amount of power, driving the demand for high-efficiency displays.[1,2] The current display technology is broadly classified into two classes: backlit and self-emissive systems.[1,3,4] A *liquid crystal display* (LCD) belongs to the first class and requires a separate backlight unit,[4,5] which not only increases the panel thickness but also restricts the flexibility and form factor.[5−7] In addition, LCDs face performance challenges such as slow response times and insufficient color saturations.[3,7] An *organic light-emitting diode* (OLED) is a widely used self-emissive display with a superior contrast ratio and flexible design. However, OLEDs have their own limitations, including burn-in problems and short operational lifetimes.[8−10] Solid-state micro-LEDs are appealing alternatives to OLEDs and LCDs in various applications.[11−13] They have many advantages such as increased brightness and reliability, reduced power consumption, longer lifetimes, and smaller form factors.[12,14−17]

Indium gallium nitride (InGaN) is a key material for micro-LED displays.[18,19] InGaN LEDs with blue emission exhibit excellent durability and *quantum efficiency* (QE).[20−23] To achieve the green or red emission required for the complete representation of color, the In concentration in InGaN must be increased. However, an increase in the In content significantly degrades the crystal quality and *internal QE* (IQE) of InGaN.[24−26] Fundamentally, the IQE degradation originates from nonradiative carrier recombination. Two main mechanisms contribute to nonradiative recombination: *Auger* and *Shockley–Read–Hall* (SRH) recombination. In Auger recombination, an electron–hole pair recombines without emission and transfers its energy to a third carrier (electron or hole).[27,28] The excited carrier relaxes through phonon scattering,

Received: March 17, 2026
Revised: May 3, 2026
Accepted: May 4, 2026
Published: May 8, 2026

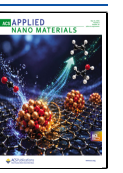

dissipating the recombination energy in the form of heat.[29] In the SRH process, point defects introduce energy states within the bandgap, which can trap electron−hole pairs that would otherwise contribute to radiative recombination.[30,31] In many cases, SRH recombination is primarily responsible for degrading the efficiency of an LED device.[32,33] In particular, deep-level defects act as the main recombination centers (Figure 1).[30,34]

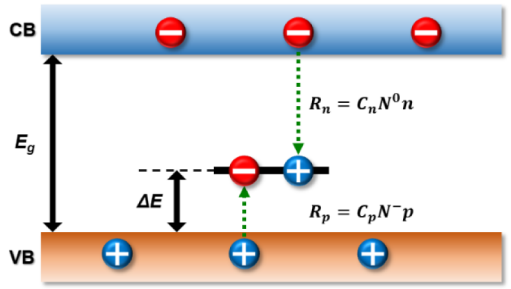

Figure 1. Schematic of the SRH recombination process at a point defect whose energy level ΔE is located above the VBM. The electron (hole) capture rate R_n (R_p) is expressed as the product of the capture coefficient C_n (C_p), carrier density n (p), and defect concentration in the charge state 0 (−1), N^0 (N^-). A deep-level defect located near the middle of the bandgap mainly contributes to the SRH recombination.

Identifying point defects and characterizing their contributions to SRH recombination can help reduce their detrimental effects on InGaN LEDs with green-to-red emissions.[35] In this respect, a first-principles study may elucidate how various types of defects influence SRH recombination rates and the overall device efficiency.[35] Nevertheless, we are unaware of any first-principles studies on the SRH recombination in InGaN. Previously, the *density functional theory* (DFT) was used to investigate point defects in GaN.[36−38] By considering native point defects (vacancies, interstitials, and antisites), Miceli and Pasquarello and Christenson et al. found that nitrogen vacancies were the most stable defects, and that carbon substitutions at N sites caused additional yellow luminescence.[39,40] Alkauskas et al. reported that the electronically excited states of defects were also important for the SRH recombination in GaN.[41]

Herein, we performed extensive DFT calculations to investigate how the SRH recombination in InGaN was affected by its composition. By systematically varying the In concentration, the emission color of $In_xGa_{1-x}N$ ($0 \le x \le 0.42$) was continuously changed from blue to green and red. We quantitatively examined the formation energies, charge transition levels, and SRH recombination rates of various substitutional and vacancy defects. It was found that the C substitution of N was the major point defect responsible for the efficiency degradation in InGaN LEDs, providing the atomic origin of the low efficiency observed in the green-to-red emission range. This fundamental understanding of the defect-induced recombination mechanism can facilitate the rational design of efficient green-to-red micro-LEDs.

■ COMPUTATIONAL METHODS

Spin-polarized DFT calculations were performed using the Vienna ab initio simulation package (VASP).[42,43] Projector augmented wave (PAW) pseudopotentials were employed to represent the core electrons.[44] The generalized gradient approximation (GGA) with the revised Perdew−Burke−Ernzerhof for solids (PBEsol) functional were utilized to describe the exchange−correlation energy.[45] The 3d electrons of Ga and In were explicitly included in the valence shell. Bandgap energies were calculated using the Heyd−Scuseria−Ernzerhof hybrid density functional (HSE06) with a fixed Hartree−Fock (HF):GGA mixing ratio of 25:75 and screening parameter of 0.2 $Å^{-1}$.[46]

The nondefective structure of $In_xGa_{1-x}N$ was built from a Wurtzite GaN unit cell. A 3 × 2 × 2 supercell composed of 48 formula units was constructed using the *special quasi-random structure* (SQS) method implemented in the alloy theoretic automated toolkit (ATAT).[47−50] By utilizing the cluster expansion up to four-body interactions, the present SQS structure emulates a random solid solution of $In_xGa_{1-x}N$. The constructed SQS represents the statistical average of local atomic environments in a random alloy. While the local compositional fluctuations (e.g., In clustering) or phase separation are not explicitly captured within this approach, it provides a reasonable description of the average defect behavior in substitutionally disordered $In_xGa_{1-x}N$. Therefore, the results in this work should be representative of those from statistically random alloys.[51,52]

The present size of supercell is commonly employed in the first-principles calculations of the defected III-nitride materials.[53−55] The previous studies have demonstrated that supercells in the range of tens to hundreds of atoms provide a reasonable balance between the computational feasibility and accuracy, especially when appropriate finite-size corrections are applied.[54,56] To mitigate the spurious defect−defect interactions arising from the periodic boundary conditions, we applied the finite-size correction scheme, which is known to effectively account for the long-range electrostatic interactions. As a result, the residual finite-size errors are expected to be significantly reduced and to decay rapidly with increasing the cell size. Regarding the alloy nature of the system, we note that the defect energetics are primarily governed by the local atomic environment surrounding the defect rather than the global configurational randomness, as reported in the previous studies on alloy semiconductors.[55] The present supercell captures the essential local coordination environments, which are the dominant factors determining the defect formation energies and transition levels. Based on these considerations, the present supercell size should provide a reasonable approximation.

We considered four types of point defects: *Ga vacancies* (V_{Ga}), *In vacancies* (V_{In}), *N vacancies* (V_N), and *C substitutions at N sites* (C_N). Each type of defect was produced by removing or substituting a single atom in the supercell while maintaining the overall charge neutrality. Only these types of defects were considered in this study because they are expected to introduce deep levels within the bandgap and directly mediate the SRH recombination. In particular, carbon is a common unintentional impurity in InGaN grown by MOCVD and MBE, originating from metal−organic precursors and residual contamination, and can incorporate at nitrogen sites to form C_N defects. Therefore, C-related defects are considered as realistic candidates for deep-level recombination centers in practical device structures. Oxygen- and hydrogen-related impurities, which are commonly incorporated during MOCVD growth, were not explicitly considered, as they are generally reported to behave as shallow donors in the Ga-based nitrides and are therefore less likely to act as efficient deep-level SRH recombination centers.[53]

Figure 2 illustrates the atomic configuration of the $In_xGa_{1-x}N$ supercell, highlighting the point defects. DFT calculations were performed at an energy cutoff of 400 eV using a gamma-centered 4 × 5 × 3 mesh to sample the Brillouin zone. To validate the present cutoff energy, we tested the cutoff energies of 450, 500, and 520 eV for all charge states of the C_N defect at x = 0.42. Figure S1 illustrates that the defect formation energies evaluated with the higher cutoff values are virtually identical to those evaluated by using the default cutoff of 400 eV (differences less than 0.005 eV). The present cutoff energy is therefore sufficient to ensure reliable and well-converged results while maintaining the computational efficiency.

The supercell geometries were relaxed until the forces were below 10 meV/Å. The defective structures were optimized by relaxing only

https://doi.org/10.1021/acsanm.6c01138
ACS Appl. Nano Mater. 2026, 9, 9478−9486

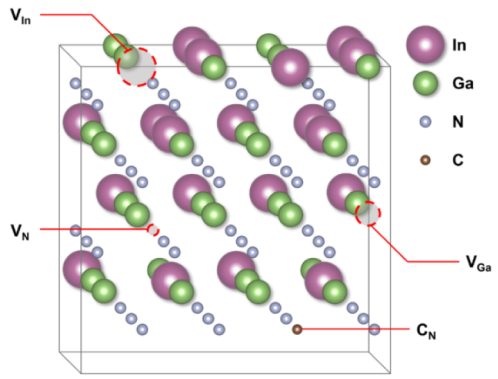

Figure 2. Four types of point defects formed in the $In_xGa_{1-x}N$ supercell. Ga, In, and N vacancies are represented by V_{Ga}, V_{In}, and V_N, respectively, and C substitution at the N site is denoted as C_N. The vacancies are indicated by the gray transparent spheres.

the ionic positions and fixing the volume to that of the nondefective supercell.[57,58]

The *formation energy* of a point defect d in the charge state q, $\Delta E_f(d;q)$ is defined as[59]

$$\Delta E_f(d;q) = G(d;q) - G(bulk) - \sum_i n_i\mu_i + q(E_{VBM} + E_F) + E_{corr} \quad (1)$$

where $G(d;q)$ and $G(bulk)$ are the energies of the defective and pristine supercells, respectively. n_i is the number of ith atoms added to or removed from the pristine material to create defects. μ_i is the chemical potential of the ith atom, E_{VBM} is the *valence band maximum* (VBM) eigenvalue of the nondefective supercell, E_F is the Fermi level, and E_{corr} is the correction term for a finite-sized supercell. All the defect formation energies were calculated by using the Spinney package.[60] The finite-size correction E_{corr} for charged defects was evaluated using the Kumagai−Oba correction scheme as implemented in Spinney, which accounts for the spurious electrostatic interactions between periodic images and includes a potential alignment correction based on atomic-site electrostatic potentials.[61] Within this framework, the correction energy is expressed as $E_{cor} = E_{lat} + q\Delta\phi$, where E_{lat} describes the electrostatic interaction between the charged defect, its periodic images, and the compensating background charge, and $\Delta\phi$ is obtained from the difference in the macroscopic average of electrostatic potentials between defective and pristine supercells.

Both the *Ga-rich* and *N-rich* conditions with $\mu_{Ga} = \mu_{Ga}(bulk)$ and $\mu_N = \mu_{N_2}$, respectively, were considered. For both conditions, the chemical potential of the other species was determined according to the thermodynamic equilibrium condition of GaN: $\mu_{GaN} = \mu_{Ga} + \mu_N$. Once μ_{Ga} and μ_N were determined, the chemical potential of In was computed via the following equation:[62]

$$\mu_{In} + \mu_{Ga} + \mu_N = \mu_{InGaN} \quad (2)$$

The chemical potential of carbon (μ_C) was referenced to the bulk carbon in its most stable phase, graphite. Since carbon is treated as an extrinsic impurity in GaN, μ_C was taken at the C-rich limit ($\mu_C = \mu_C^{graphite}$), without defining separate C-rich and C-poor conditions. This choice provides the upper bound of μ_C and is consistent with standard defect formalisms. The chemical potentials were further constrained to ensure the thermodynamic stability of the host GaN under Ga-rich and N-rich conditions, while avoiding the formation of competing secondary phases involving carbon.[63]

The nonradiative *capture coefficient* $C_{n,p}$ was calculated using the configuration coordinate model within an effective one-dimensional (1D) phonon approximation.[35,41,64] In this approach, multidimensional lattice vibrations are projected onto a single effective mode that captures the dominant structural relaxation associated with carrier capture. While this approximation significantly reduces computational cost, it neglects contributions from multiple phonon modes and possible anharmonic effects. These limitations may be more pronounced in disordered alloy systems such as InGaN, where local structural variations broaden the phonon spectrum and introduce additional coupling channels. Nevertheless, the carrier capture process is typically dominated by localized defect states and their associated lattice relaxation, making the 1D approximation a reasonable approach for capturing the primary physics of nonradiative recombination. Therefore, the calculated capture coefficients are expected to reliably describe relative trends across different compositions, although their absolute values may carry some uncertainty. The carrier capture coefficient is given by

$$C_{\{n,p\}}(T) = Vf\eta_{sp}g\left(\frac{2\pi}{\hbar}\right)W_{if}^2 \sum_{m,n} \omega_m(T)|\langle\chi_{im}|Q + \Delta Q|\chi_{fn}\rangle|^2 \times \delta(\Delta E + m\hbar\Omega_i - n\hbar\Omega_f) \quad (3)$$

where V is the supercell volume, f is the scaling factor describing the capture by charged defects, g is the degeneracy of the final state, and W_{if} is the electron−phonon coupling matrix element. η_{sp} reflects the spin-selection rules ($\eta_{sp} = 1$ when the initial state is a spin singlet and the final state is a doublet; $\eta_{sp} = 1/2$ when the initial state is a spin doublet and the final spin is a singlet). ΔE is the energy difference between the two states; Ω_i and Ω_f are the effective vibrational frequencies in the initial and the final state, respectively; and Q is the effective one-dimensional phonon coordinate ($Q = 0$ corresponds to the equilibrium geometry of the initial state). The potential energy minima of the two electronic states are offset by ΔQ. The sum runs over the vibrational states of the excited (χ_{im}) and ground (χ_{fn}) electronic states. $\omega_m(T)$ is the thermal occupation factor. The delta functions are replaced by Gaussians with a standard deviation of $0.8\hbar\Omega_f$.

RESULTS AND DISCUSSION

The DFT calculations yielded the following GaN lattice parameters: $a = 3.16$ Å and $c = 5.15$ Å, which closely match the experimental values $a = 3.19$ Å and $c = 5.19$ Å.[65] The lattice parameters of $In_xGa_{1-x}N$ determined for $x = 0.04$, 0.17, 0.25, and 0.42 are $a = 3.18$, 3.22, 3.25, and 3.30 Å, and $c = 5.18$, 5.24, 5.28, and 5.35 Å, respectively. The observed increase in the lattice parameter with increasing the *fraction of* In, x, can be attributed to the fact that the In atom is bigger in size than the Ga atom. Considering the lattice parameters of InN ($a = 3.55$ Å, $c = 5.70$ Å),[66] the calculated lattice parameters are reasonable.

Figure 3 shows the bandgap energy of $In_xGa_{1-x}N$ plotted as a function of x. Regardless of the utilized functional, the bandgap energy decreases as x increases from 0 to 0.42. The experimental bandgap energy of GaN (3.50 eV) is significantly underestimated using the PBEsol functional (2.01 eV). However, the bandgap energies obtained with the HSE06 functional agree well with the experimental data:[40,67,68] the bandgap energy of GaN is 3.52 eV, which closely matches the previously computed[56] and experimental values. In addition, the HSE06 calculated bandgap energies are in good agreement with the experimental values reported for $x = 0.05$ (3.25 eV) and 0.11 (3.01 eV).[69] Figure 3 also shows the wavelengths and colors corresponding to the bandgap energies. The wavelength increases from 352 to 373, 448, 492, and 579 nm as x increases from 0 to 0.04, 0.17, 0.25, and 0.42, respectively. These wavelengths cover the entire visible (blue to red) color spectrum. It should be noted that the actual emission from an InGaN LED slightly differs from the bandgap wavelength reported here. Approximately, however, with increasing x from

https://doi.org/10.1021/acsanm.6c01138
ACS Appl. Nano Mater. 2026, 9, 9478−9486

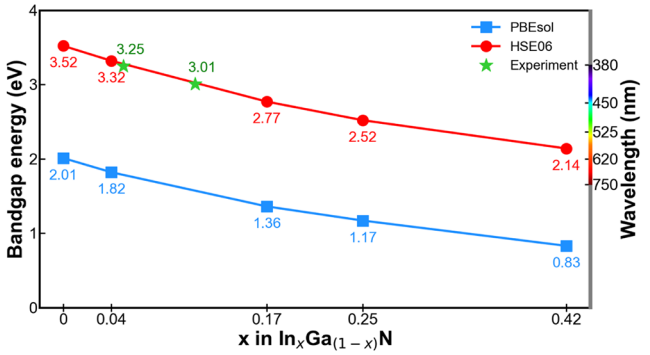

Figure 3. Bandgap energy versus the fraction of In, x, in $In_xGa_{1-x}N$. The obtained values were computed by employing the PBEsol (squares) and HSE06 (circles) functionals. The experimental values obtained for x = 0.05 and 0.11 are presented as stars. In the right y axis, the wavelength and color of the visible spectrum are shown for reference. The lines serve as visual guides.

0 to 0.42, the emission color of $In_xGa_{1-x}N$ changes from blue to green and red.[70,71]

In a practical InGaN-based LED, a nanoscale layer of InGaN is typically grown on a GaN substrate, resulting in the in-plane lattice constants constrained to those of GaN.[72] To evaluate the effect of such a strain, we calculated the bandgap under the strained conditions by fixing the in-plane lattice parameters to those of GaN (Figure S2). For example, at the composition of 42% In, the bandgap decreased from 2.14 to 1.82 eV by introducing the strain. The reduced bandgap under the strain may facilitate the carrier capture processes and therefore the SRH recombination rate could be somewhat enhanced compared to that of the relaxed structure. Despite this difference, the overall trend of reduction in the bandgap with increasing the fraction of In remained unchanged (Figure S2).

First, we inspected point defects in GaN. Figure 4 plots the defect formation energy versus the Fermi energy. For each

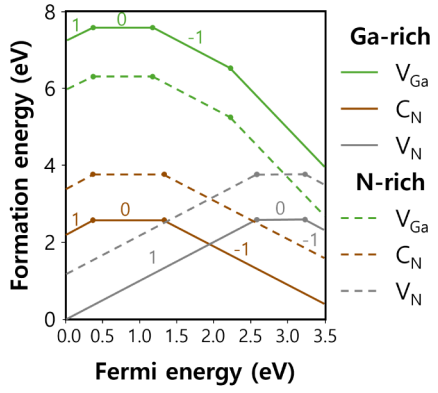

Figure 4. Defect formation energy of GaN plotted as a function of the Fermi energy under the Ga-rich (solid lines) and N-rich (broken lines) conditions. Results are shown for V_{Ga} (green), V_N (gray), and C_N (brown) defects, whose charge states are listed above each curve. The kinks of each curve correspond to charge transition levels.

curve, only the lowest energy among the different charge states is shown (see eq 1). These results are obtained for three types of defects under the Ga-rich and N-rich conditions. Throughout this paper, all Fermi energies are reported relative to the VBM calculated using the HSE06 method. The formation energies of defects with different charge states evaluated at the VBM (Fermi energy = 0) are listed in Table 1. In order to verify the convergence of the considered charge

Table 1. Formation Energies of Various Point Defects ΔE_f s in GaN Calculated under the Ga-Rich and N-Rich Chemical Potential Conditions[a]

		ΔE_f (eV)	
Defect	Charge State	Ga-rich	N-rich
V_{Ga}	+1	7.19	5.98
	0	7.54	6.33
	−1	8.73	7.52
	−2	10.95	9.74
	−3	14.44	13.24
V_N	+3	0.83	2.04
	+2	0.19	1.40
	+1	−0.01	1.20
	0	2.58	3.79
	−1	5.81	7.02
C_N	+3	3.38	4.58
	+2	2.46	3.67
	+1	2.17	3.38
	0	2.56	3.77
	−1	3.90	5.11

[a] V_{Ga}, V_N, and C_N defects are considered. The ΔE_f values obtained at the Fermi energy equal to zero (at the VBM) are presented in Figure 4.

states, we performed additional calculations for the higher and lower charge states for all the defects.[63,73−76] The results show that the formation energies of extreme charge states are consistently higher than those of intermediate states across the entire Fermi level range. In particular, the −2 charge states of C_N and V_N, as well as the +3 charge states of V_{Ga} and V_{In}, are always less stable than neighboring charge states, confirming that the relevant charge states are well converged. The corresponding formation energy diagrams are illustrated in the Supporting Information Figure S3.

Figure 4 shows that regardless of the defect type, the formation energy linearly increases (q = 1), plateaus (q = 0), and decreases (q = −1) as the Fermi level moves up from the VBM toward the *conduction band minimum* (CBM). In the neutral-charge state (q = 0), V_{Ga} defects have the highest formation energy. The formation energies of V_N and C_N defects are comparable. By switching from the Ga-rich to N-rich condition, the formation energy of V_{Ga} defects decreases, but those of V_N and C_N defects increase (Figure 4), which is consistent with the study conducted by Miceli and Pasquarello.[40] Transition levels within the bandgap of GaN were determined for the $V_{Ga}(1/0)$, $V_{Ga}(0/-1)$, $C_N(1/0)$, $C_N(0/-1)$, $V_N(1/0)$, and $V_N(0/-1)$ defects. The formation energies of the neutral states of V_{Ga} (7.54 eV) and V_N (2.58 eV) defects under the Ga-rich condition (Table 1) are in good agreement with the prior values (7.02 and 2.59 eV) obtained from the results of full hybrid functional calculations.[40,57] This further validates the present method combining the PBEsol functional for the structure optimization with the HSE06 bandgap calculation.

Next, we examined various defects in $In_xGa_{1-x}N$ (x = 0.04, 0.17, 0.25, and 0.42), as shown in Figure 5. Here, the formation energies of V_{Ga}, C_N, and V_N defects exhibit trends qualitatively similar to those observed for GaN; V_{Ga} defects generally have higher formation energies than those of C_N and

https://doi.org/10.1021/acsanm.6c01138
ACS Appl. Nano Mater. 2026, 9, 9478−9486

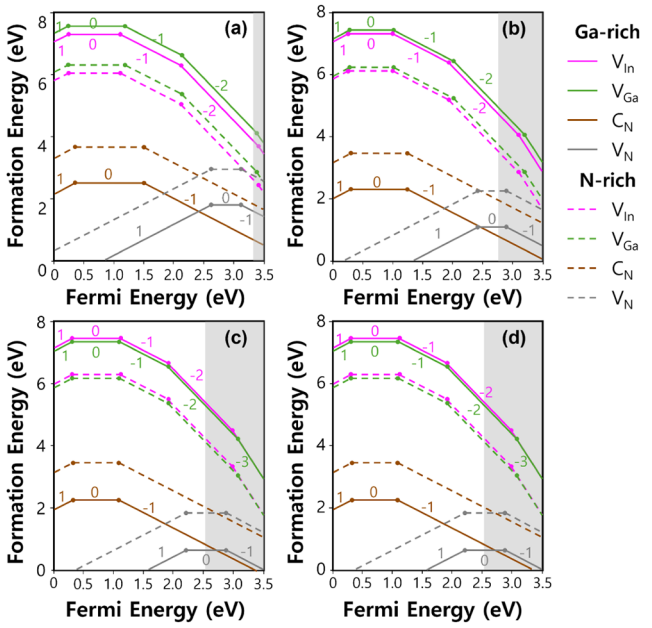

Figure 5. Formation energies of the point defects in $In_xGa_{1-x}N$. x is varied as x = 0.04 (a), 0.17 (b), 0.25 (c), and 0.42 (d). As the In fraction x increases, the bandgap (white area) shrinks, and the conduction band region (gray area) widens.

V_N defects. The formation energy of C_N defects, which was lower than that of GaN, decreases slightly with increasing In fraction. The formation energies of V_N defects are considerably lower than those of C_N, especially at high In fractions. The formation energy of V_N defects significantly decreases with increasing x, whereas that of C_N defects exhibits no pronounced variations with x. The newly introduced V_{In} defects have formation energies close to those of V_{Ga} defects (within 0.35 eV) regardless of the In fraction. The formation energies of V_{Ga} and V_{In} defects vary only slightly with x under both the Ga-rich and N-rich conditions. Note that with raising In fraction, the bandgap region shrinks as the CB (drawn as a gray area) broadens with the CBM approaching 2.14 eV for x = 0.42. Consequently, some transition levels, such as the $V_N(0/-1)$ level, disappear from the bandgap region.

In Figure 6, the charge transition levels of defects in $In_xGa_{1-x}N$ are plotted as functions of x, and the obtained results are shown for the cationic (Ga and In, top) and anionic (N, bottom) site defects. The numbers near the symbols represent the Fermi energies of the corresponding transition levels. Only the transition levels within the bandgap region are displayed. According to Figure 6 (top), V_{Ga} and V_{In} transition levels have similar Fermi energies, consistent with Figure 5. The $V_{Ga}(-2/-3)$ level of $In_xGa_{1-x}N$ is very close to that of the CBM for x = 0 (GaN) and rapidly disappears from the bandgap region as x increases to 0.04. The $(-1/-2)$ levels of V_{Ga} and V_{In} defects are closer to the CBM than to the VBM

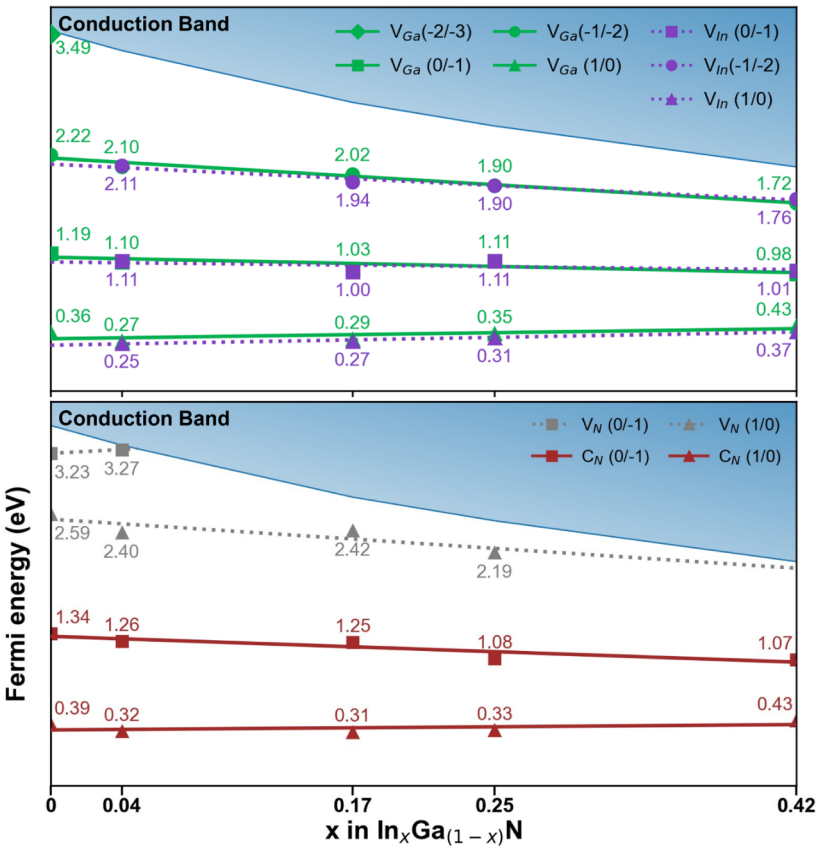

Figure 6. Charge transition levels of the cationic (top) and anionic (bottom) site defects plotted as functions of the In fraction x in $In_xGa_{1-x}N$. Each number near a symbol indicates the Fermi energy of a specific charge transition level measured from the VBM. The conduction band is shown as the blue area. In the top part, the transition levels of the V_{Ga} (V_{In}) defects are represented by the green (purple) symbols. In the bottom part, the transition levels of the C_N (V_N) defects are denoted by the red (gray) symbols. All lines represent the linear regressions of the transition levels with respect to x. The same axis labels displayed in the bottom apply to the top panel.

https://doi.org/10.1021/acsanm.6c01138
ACS Appl. Nano Mater. 2026, 9, 9478−9486

and shift even closer to the CBM as x increases. However, the (1/0) levels of V_{Ga} and V_{In} defects are close (within 0.4 eV) to that of the VBM regardless of x. The (0/−1) levels of V_{Ga} and V_{In} defects are located near the middle of the bandgap but slightly closer to the VBM. Note that the (1/0) and (0/−1) levels of V_{Ga} and V_{In} defects remain nearly unchanged (within 0.12 eV) with varying x. The (−1/−2) transition level is shifted significantly toward the CBM as x increases.

As shown in Figure 5, V_N defects exhibit the lowest formation energy. However, at x = 0.42, the $V_N(1/0)$ and $V_N(0/-1)$ levels are located outside the bandgap and, therefore, unlikely to cause an SRH recombination. As illustrated in Figure 6 (bottom), the $V_N(0/-1)$ level is present inside the bandgap only at x = 0 and 0.04. The $V_N(1/0)$ level appears in the bandgap at x = 0−0.25. At high In content ($x \approx$ 0.42), the V_N defect levels approach the conduction band edge and no longer form localized deep levels within the bandgap, indicating a transition to a shallow (or resonant) donor.[53,77] This implies that electrons associated with V_N can be more readily thermally activated into the conduction band, potentially increasing the free-electron concentration. This might contribute to a native n-type conductivity at a high In content. V_N does not always dominate an unintentional n-type conductivity in III-nitrides, and other donors or impurities, such as oxygen, might play a significant role.

Both the $C_N(1/0)$ and $C_N(0/-1)$ transition levels remain within the bandgap for the entire range of x. Although the $V_{Ga}(1/0)$, $V_{In}(1/0)$, and $C_N(1/0)$ transition levels exist within the bandgap at all In fractions, these transition levels are close to the VBM and, therefore, unlikely to be deep acceptors. In contrast, the $C_N(0/-1)$ transition level remains within the bandgap across the entire composition range. The $V_{Ga}(0/-1)$, $V_{In}(0/-1)$, and $C_N(0/-1)$ transition levels are potential deep acceptors; however, the formation energies of the $V_{Ga}(0/-1)$ and $V_{In}(0/-1)$ levels are much higher than that of $C_N(0/-1)$. Therefore, the $C_N(0/-1)$ defect type is the most probable deep acceptor.

After identifying the $C_N(0/-1)$ defect as the main deep acceptor for SRH recombination, we calculated the electron (C_n) and hole (C_p) capture coefficients for $C_N(0/-1)$ defects in $In_xGa_{1-x}N$. In the case of GaN, we obtained $C_p = 1.94 \times 10^{-10}$ cm^3/s, which is comparable to but slightly smaller than the previously computed values 3.1×10^{-9} cm^3/s.[64] The C_p and C_n values computed for the $C_N(0/-1)$ in $In_xGa_{1-x}N$ exhibit a clear dependence on the In concentration: at x = 0.04, C_p and C_n are equal to 9.77×10^{-9} and 2.19×10^{-13} cm^3/s, respectively. Upon increasing x to 0.17, 0.25, and 0.42, C_p (C_n) varied as 3.32×10^{-8} (2.08×10^{-12}), 4.09×10^{-8} (3.77×10^{-12}) and 2.78×10^{-8} (6.03×10^{-10}) cm^3/s, respectively. In all compositions, C_p is significantly larger than C_n, indicating that the recombination process is limited by the electron capture. The SRH recombination rate R is expressed by the following formula:

$$R = N_T \frac{C_n C_p np}{C_n n + C_p p} \tag{4}$$

where N_T denotes the defect concentration, and n and p are the electron and hole concentrations, respectively. Under the high-injection condition with $n \approx p$, eq 4 is simplified to $R = An$, where the *SRH coefficient* A is expressed as $A = N_T C_{tot}$, and the total capture coefficient C_{tot} is computed via the formula $C_{tot} = \frac{C_n C_p}{C_n + C_p}$.[41]

We use a constant defect concentration N_T of 1.00×10^{16} cm^{-3}, which lies within the experimentally reported range of defect densities in InGaN. This value is consistent with values adopted in previous first-principles studies.[19,32,41,78] Note however the SRH coefficient linearly scales with N_T, and N_T can change with varying the In fraction x. In practical InGaN devices, increasing the In content is often accompanied by enhanced strain, alloy disorder, and defect incorporation, which can lead to an increase in N_T.[79,80] When such composition-dependent defect densities are considered, the SRH recombination would be further enhanced at higher In concentrations. Therefore, the efficiency degradation predicted in this work should be regarded as a lower-bound estimate, and more severe degradation is expected in real devices.[81]

In Figure 7, the SRH recombination coefficient A is plotted as a function of the In fraction x. As shown in Figure 7, the

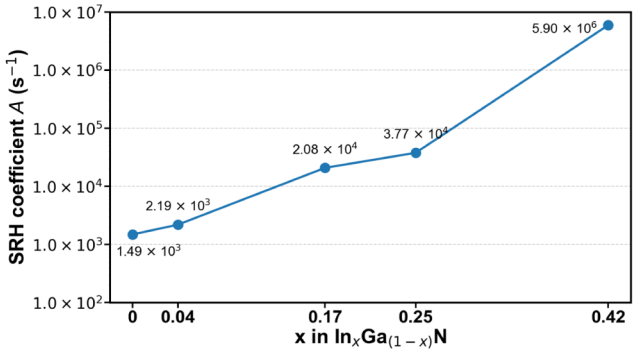

Figure 7. SRH recombination coefficient A plotted as a function of the In fraction x in $In_xGa_{1-x}N$. The values are calculated for the dominant deep-level defects $C_N(0/-1)$, assuming a defect concentration of 1.0×10^{16} cm^{-3}.

SRH coefficient A increases with increasing the In content. With increasing x from 0 to 0.42, A increases by more than 3 orders of magnitude. This shows a strong composition dependence of the electron capture process associated with the $C_N(0/-1)$ defect, suggesting that SRH recombination becomes increasingly significant at a higher In concentration. The A coefficient should be interpreted as the contribution of the considered defect channel, rather than the total effective A coefficient governing a device-level IQE behavior. Also, the radiative and Auger recombinations should be considered to assess the overall efficiency of an InGaN LED.

Admittedly, a nanoscale layer of InGaN is typically grown on a GaN substrate and the in-plane lattice constants are likely to be constrained to those of GaN. The reduced bandgap under the strain due to a substrate of InGaN (typically GaN) may facilitate the carrier capture processes and therefore the SRH recombination could be somewhat enhanced compared to the relaxed case. Therefore, the present results based on the relaxed structures of InGaN slightly underestimate the actual SRH processes in the real devices. In Figure S2, the bandgap values of both the relaxed and strained structures are plotted vs the In fraction.

CONCLUSION

InGaN LEDs exhibit distinct advantages over OLEDs and LCDs, such as enhanced stability, lifetime, and brightness. However, the QE of InGaN LEDs with green-to-red emission is relatively poor and desired to be improved. Such an

https://doi.org/10.1021/acsanm.6c01138
ACS Appl. Nano Mater. 2026, 9, 9478−9486

improvement should be based on the fundamental understanding of the nonradiative recombination mechanism underlying the low efficiency of InGaN with green-to-red emission. By performing first-principles calculations, we investigated various point defects and their impacts on the SRH recombination in an InGaN LED. By systematically varying the InGaN composition, we elucidated the influences of various defects on carrier recombination and the overall device efficiency by examining the formation energies and transition levels. The incorporation of In into GaN facilitated the formation of Ga and In vacancies and C substitution of N sites, and this trend became more pronounced with increasing In content. The C substitution of N sites resulted in the most pronounced SRH recombination. Based on our defect formation energy analysis, Ga-rich conditions are expected to suppress the formation of C_N defects. In practical growth processes, such conditions can be achieved by adjusting the V/III ratio, which controls the effective chemical potentials during epitaxy.[82,83] The SRH recombination coefficient A was found to increase by 3 orders of magnitude with raising the In content from 0 to 42%. This trend, primarily driven by the composition-dependent electron capture process of C_N defects, suggests that defect-mediated SRH recombination becomes increasingly significant in the high-In InGaN alloy. Our findings underscore the importance of controlling point defects to mitigate the efficiency losses of InGaN LEDs with green-to-red emissions. The oxygen- and hydrogen-related impurities, which are commonly incorporated in a MOCVD growth, were not explicitly considered in this study. Although they are generally associated with shallow donor behavior, they may still influence recombination indirectly through changes in carrier concentration or interactions with native defects. The present study focused on the defect-mediated SRH recombination from an atomistic viewpoint provided by the first-principles calculation. It should be noted, however, according to the venerable ABC model,[84−86] the overall IQE is influenced by the radiative and Auger recombinations as well. In particular, the Auger recombination is known to become significant at high carrier injection levels.[27,84,87] Therefore, the conclusions of this study are limited to defect-mediated SRH processes, and the contributions of other recombination channels may vary depending on the operating conditions. A comprehensive analysis including all recombination mechanisms is left as a future work.

■ ASSOCIATED CONTENT

Supporting Information

The Supporting Information is available free of charge at https://pubs.acs.org/doi/10.1021/acsanm.6c01138.

Formation energies of the CN defects (with three different charges) evaluated by using different cutoff values for the plane-wave energy (x = 0.42); Calculated bandgap energies of $In_xGa_{1-x}N$ as a function of the In fraction x for both the bulk and strained structures (Figure S2); defect formation energies as a function of Fermi level for various charge states of intrinsic defects in $In_xGa_{1-x}N$ at different In compositions (x = 0.04 and 0.17) (Figure S3) (PDF)

■ AUTHOR INFORMATION

Corresponding Authors

Sung-Chan Jo − *Samsung Display Co., Ltd., Yongin-si, Gyeonggi-do 17113, Republic of Korea*; Email: enigma.jo@samsung.com

Joonkyung Jang − *Department of Nanoenergy Engineering, Pusan National University, Busan 46241, Republic of Korea*; orcid.org/0000-0001-9028-0605; Email: jkjang@pusan.ac.kr

Authors

Kisang Byun − *Department of Nanoenergy Engineering, Pusan National University, Busan 46241, Republic of Korea*; orcid.org/0000-0001-6648-2792

Arindam Sannyal − *Department of Nanoenergy Engineering, Pusan National University, Busan 46241, Republic of Korea*; orcid.org/0000-0002-8376-7017

Dohee Kim − *Department of Nanoenergy Engineering, Pusan National University, Busan 46241, Republic of Korea*; orcid.org/0000-0003-2942-5312

Sang Ho Jeon − *Samsung Display Co., Ltd., Yongin-si, Gyeonggi-do 17113, Republic of Korea*; orcid.org/0000-0001-8280-3808

Complete contact information is available at: https://pubs.acs.org/10.1021/acsanm.6c01138

Notes

The authors declare no competing financial interest.

■ ACKNOWLEDGMENTS

This work was supported by Samsung Display Co., Ltd. It was also supported by the Industrial Technology Innovation Program (RS-2024-00435432, Development of hydrogen production technology through ammonia decomposition using a plasmonics-based light system with high performance and long-term durability) funded By the Ministry of Trade Industry & Energy (MOTIE, Korea) and by the Basic Science Research Program through the National Research Foundation of Korea (NRF) funded by the Ministry of Education (RS-2025-02653508).

■ REFERENCES

(1) Wierer, J. J., Jr; Tansu, N. III-Nitride micro-LEDs for efficient emissive displays. *Laser Photonics Rev.* **2019**, *13* (9), 1900141.

(2) Rodriguez Fernandez, M.; Zalama Casanova, E.; Gonzalez Alonso, I. Review of display technologies focusing on power consumption. *Sustainability* **2015**, *7* (8), 10854−10875.

(3) Wu, T.; Sher, C.-W.; Lin, Y.; Lee, C.-F.; Liang, S.; Lu, Y.; Huang Chen, S.-W.; Guo, W.; Kuo, H.-C.; Chen, Z. Mini-LED and micro-LED: promising candidates for the next generation display technology. *Appl. Sci.* **2018**, *8* (9), 1557.

(4) Armitage, D.; Underwood, I.; Wu, S.-T. *Introduction to microdisplays*; John Wiley & Sons, 2006.

(5) Cuervo, E.; Chintalapudi, K.; Kotaru, M. Creating the perfect illusion: What will it take to create life-like virtual reality headsets? In *Proceedings of the 19th international workshop on mobile computing systems and applications*. ACM, Inc. 2018; pp 7−12.

(6) Bhowmik, A. K.; Li, Z.; Bos, P. J. *Mobile displays: Technology and applications*; John Wiley & Sons, 2008.

(7) Schadt, M. Milestone in the history of field-effect liquid crystal displays and materials. *Jpn. J. Appl. Phys.* **2009**, *48* (3S2), 03B001.

(8) Tang, C. W.; Van Slyke, S. A. Organic electroluminescent diodes. *Appl. Phys. Lett.* **1987**, *51* (12), 913−915.

(9) Kim, K.-H.; Lee, S.; Moon, C.-K.; Kim, S.-Y.; Park, Y.-S.; Lee, J.-H.; Woo Lee, J.; Huh, J.; You, Y.; Kim, J.-J. Phosphorescent dye-based supramolecules for high-efficiency organic light-emitting diodes. *Nat. Commun.* **2014**, *5* (1), 4769.
(10) Lee, J.-H.; Chen, C.-H.; Lee, P.-H.; Lin, H.-Y.; Leung, M.-K.; Chiu, T.-L.; Lin, C.-F. Blue organic light-emitting diodes: current status, challenges, and future outlook. *J. Mater. Chem. C* **2019**, *7* (20), 5874−5888.
(11) Huang, Y.; Hsiang, E.-L.; Deng, M.-Y.; Wu, S.-T. Mini-LED, Micro-LED and OLED displays: present status and future perspectives. *Light Sci. Appl.* **2020**, *9* (1), 105.
(12) Park, H. K.; Yoon, S. W.; Eo, Y. J.; Chung, W. W.; Yoo, G. Y.; Oh, J. H.; Lee, K. N.; Kim, W.; Do, Y. R. Horizontally assembled green InGaN nanorod LEDs: scalable polarized surface emitting LEDs using electric-field assisted assembly. *Sci. Rep.* **2016**, *6* (1), 28312.
(13) Huang, Y.; Tan, G.; Gou, F.; Li, M. C.; Lee, S. L.; Wu, S. T. Prospects and challenges of mini-LED and micro-LED displays. *J. Soc. Inf. Dispersion* **2019**, *27* (7), 387−401.
(14) Smith, J. M.; Ley, R.; Wong, M. S.; Baek, Y. H.; Kang, J. H.; Kim, C. H.; Gordon, M. J.; Nakamura, S.; Speck, J. S.; DenBaars, S. P. Comparison of size-dependent characteristics of blue and green InGaN microLEDs down to 1 μm in diameter. *Appl. Phys. Lett* **2020**, *116* (7), 071102.
(15) Tian, P.; McKendry, J. J.; Gong, Z.; Guilhabert, B.; Watson, I. M.; Gu, E.; Chen, Z.; Zhang, G.; Dawson, M. D. Size-dependent efficiency and efficiency droop of blue InGaN micro-light emitting diodes. *Appl. Phys. Lett.* **2012**, *101* (23), 231110.
(16) Jiang, H.; Jin, S.; Li, J.; Shakya, J.; Lin, J. III-nitride blue microdisplays. *Appl. Phys. Lett.* **2001**, *78* (9), 1303−1305.
(17) Park, S.-I.; Xiong, Y.; Kim, R.-H.; Elvikis, P.; Meitl, M.; Kim, D.-H.; Wu, J.; Yoon, J.; Yu, C.-J.; Liu, Z. Printed assemblies of inorganic light-emitting diodes for deformable and semitransparent displays. *Science* **2009**, *325* (5943), 977−981.
(18) Karpov, S. Y. Carrier localization in InGaN by composition fluctuations: implication to the "green gap". *Photon. Res.* **2017**, *5* (2), A7−A12.
(19) Auf der Maur, M.; Pecchia, A.; Penazzi, G.; Rodrigues, W.; Di Carlo, A. Efficiency drop in green InGaN/GaN light emitting diodes: The role of random alloy fluctuations. *Phys. Rev. Lett.* **2016**, *116* (2), 027401.
(20) Yamada, M.; Mitani, T.; Narukawa, Y.; Shioji, S.; Niki, I.; Sonobe, S.; Deguchi, K.; Sano, M.; Mukai, T. InGaN-Based Near-Ultraviolet and Blue-Light-Emitting Diodes with High External Quantum Efficiency Using a Patterned Sapphire Substrate and a Mesh Electrode. *Jpn. J. Appl. Phys.* **2002**, *41*, L1431−L1433.
(21) Jafar, N.; Jiang, J.; Lu, H.; Qasim, M.; Zhang, H. Recent Research on Indium-Gallium-Nitride-Based Light-Emitting Diodes: Growth Conditions and External Quantum Efficiency. *Crystals* **2023**, *13* (12), 1623.
(22) Hall, R. N. Electron-hole recombination in germanium. *Phys. Rev.* **1952**, *87* (2), 387.
(23) Feezell, D.; Nakamura, S. Invention, development, and status of the blue light-emitting diode, the enabler of solid-state lighting. *C. R. Phys.* **2018**, *19* (3), 113−133.
(24) Karpov, S. Y. Effect of carrier localization on recombination processes and efficiency of InGaN-based LEDs operating in the "Green Gap". *Appl. Sci.* **2018**, *8* (5), 818.
(25) Chen, D.; Wang, Z.; Hu, F.-C.; Shen, C.; Chi, N.; Liu, W.; Zhang, D. W.; Lu, H.-L. Improved electro-optical and photoelectric performance of GaN-based micro-LEDs with an atomic layer deposited AlN passivation layer. *Opt. Express* **2021**, *29* (22), 36559−36566.
(26) Huang, M.; Li, H.; Chen, S. Triple-Site Dopant−Defect Complexes in Mg−H-Codoped GaN: First-Principles Identification. *Phys. Status Solidi A* **2021**, *218* (7), 2000723.
(27) Delaney, K. T.; Rinke, P.; Van de Walle, C. G. Auger recombination rates in nitrides from first principles. *Appl. Phys. Lett.* **2009**, *94* (19), 191109.
(28) Kioupakis, E.; Rinke, P.; Delaney, K. T.; Van de Walle, C. G. Indirect Auger recombination as a cause of efficiency droop in nitride light-emitting diodes. *Appl. Phys. Lett.* **2011**, *98* (16), 161107.
(29) Achermann, M.; Bartko, A. P.; Hollingsworth, J. A.; Klimov, V. I. The effect of Auger heating on intraband carrier relaxation in semiconductor quantum rods. *Nat. Phys.* **2006**, *2* (8), 557−561.
(30) Bulashevich, K. A.; Karpov, S. Y. Impact of surface recombination on efficiency of III-nitride light-emitting diodes. *Phys. Status Solidi RRL* **2016**, *10* (6), 480−484.
(31) Schubert, E. F. *Light-emitting diodes*; Cambridge university press, 2006.
(32) Schiavon, D.; Binder, M.; Peter, M.; Galler, B.; Drechsel, P.; Scholz, F. Wavelength-dependent determination of the recombination rate coefficients in single-quantum-well GaInN/GaN light emitting diodes. *Phys. Status Solidi B* **2013**, No. 2, 250.
(33) Eliseev, P. G.; Osin'ski, M.; Li, H.; Akimova, I. V. Recombination balance in green-light-emitting GaN/InGaN/AlGaN quantum wells. *Appl. Phys. Lett.* **1999**, *75* (24), 3838−3840.
(34) Henry, C.; Lang, D. V. Nonradiative capture and recombination by multiphonon emission in GaAs and GaP. *Phys. Rev. B* **1977**, *15* (2), 989.
(35) Turiansky, M. E.; Alkauskas, A.; Engel, M.; Kresse, G.; Wickramaratne, D.; Shen, J.-X.; Dreyer, C. E.; Van de Walle, C. G. Nonrad: Computing nonradiative capture coefficients from first principles. *Comput. Phys. Commun.* **2021**, *267*, 108056.
(36) Neugebauer, J.; Van de Walle, C. G. Atomic geometry and electronic structure of native defects in GaN. *Phys. Rev. B* **1994**, *50* (11), 8067.
(37) Bogusl, P.; Briggs, E. L.; Bernholc, J. Native defects in gallium nitride. *Phys. Rev. B* **1995**, *51* (23), 17255.
(38) Limpijumnong, S.; Van de Walle, C. G. Diffusivity of native defects in GaN. *Phys. Rev. B* **2004**, *69* (3), 035207.
(39) Christenson, S. G.; Xie, W.; Sun, Y.; Zhang, S. Carbon as a source for yellow luminescence in GaN: Isolated CN defect or its complexes. *J. Appl. Phys.* **2015**, *118* (13), 135708.
(40) Miceli, G.; Pasquarello, A. Energetics of native point defects in GaN: A density-functional study. *Microelectron. Eng.* **2015**, *147*, 51−54.
(41) Alkauskas, A.; Dreyer, C. E.; Lyons, J. L.; Van de Walle, C. G. Role of excited states in Shockley-Read-Hall recombination in wide-band-gap semiconductors. *Phys. Rev. B* **2016**, *93* (20), 201304.
(42) Kresse, G.; Furthmüller, J. Efficient iterative schemes for ab initio total-energy calculations using a plane-wave basis set. *Phys. Rev. B* **1996**, *54* (16), 11169.
(43) Kresse, G.; Joubert, D. From ultrasoft pseudopotentials to the projector augmented-wave method. *Phys. Rev. B* **1999**, *59* (3), 1758.
(44) Blöchl, P. E. Projector augmented-wave method. *Phys. Rev. B* **1994**, *50* (24), 17953.
(45) Perdew, J. P.; Ruzsinszky, A.; Csonka, G. I.; Vydrov, O. A.; Scuseria, G. E.; Constantin, L. A.; Zhou, X.; Burke, K. Restoring the density-gradient expansion for exchange in solids and surfaces. *Phys. Rev. Lett.* **2008**, *100* (13), 136406.
(46) Deák, P.; Aradi, B.; Frauenheim, T. Polaronic effects in TiO 2 calculated by the HSE06 hybrid functional: Dopant passivation by carrier self-trapping. *Phys. Rev. B* **2011**, *83* (15), 155207.
(47) Hart, G. L.; Forcade, R. W. Algorithm for generating derivative structures. *Phys. Rev. B* **2008**, *77* (22), 224115.
(48) Van de Walle, A.; Ceder, G.; Waghmare, U. First-principles computation of the vibrational entropy of ordered and disordered Ni 3 Al. *Phys. Rev. Lett.* **1998**, *80* (22), 4911.
(49) Von Pezold, J.; Dick, A.; Friák, M.; Neugebauer, J. Generation and performance of special quasirandom structures for studying the elastic properties of random alloys: Application to Al-Ti. *Phys. Rev. B* **2010**, *81* (9), 094203.
(50) van de Walle, A.; Tiwary, P.; de Jong, M.; Olmsted, D. L.; Asta, M.; Dick, A.; Shin, D.; Wang, Y.; Chen, L.-Q.; Liu, Z.-K. Efficient stochastic generation of special quasirandom structures. *Calphad* **2013**, *42*, 13−18.

https://doi.org/10.1021/acsanm.6c01138
ACS Appl. Nano Mater. 2026, 9, 9478−9486

(51) Lee, C.-W.; Din, N. U.; Yazawa, K.; Nemeth, W.; Smaha, R. W.; Haegel, N. M.; Gorai, P. Defect control strategies for Al1− xGdxN alloys. *J. Appl. Phys.* **2024**, *135* (15), 155101.
(52) Schultz, P. A. Modeling neutral defects in III-V ternary alloys with a special quasirandom structure: Analysis of As-and III-site point defects in InGaAs. *Phys. Rev. B* **2025**, *112* (9), 094112.
(53) Van de Walle, C. G.; Neugebauer, J. First-principles calculations for defects and impurities: Applications to III-nitrides. *J. Appl. Phys.* **2004**, *95* (8), 3851−3879.
(54) Lany, S.; Zunger, A. Accurate prediction of defect properties in density functional supercell calculations. *Modell. Simul. Mater. Sci. Eng.* **2009**, *17* (8), 084002.
(55) Zunger, A.; Wei, S.-H.; Ferreira, L. G.; Bernard, J. E. Special quasirandom structures. *Phys. Rev. Lett.* **1990**, *65* (3), 353.
(56) Lyons, J.; Janotti, A.; Van de Walle, C. Effects of carbon on the electrical and optical properties of InN, GaN, and AlN. *Phys. Rev. B* **2014**, *89* (3), 035204.
(57) Deák, P.; Lorke, M.; Aradi, B.; Frauenheim, T. Carbon in GaN: Calculations with an optimized hybrid functional. *Phys. Rev. B* **2019**, *99* (8), 085206.
(58) Goyal, A.; Gorai, P.; Peng, H.; Lany, S.; Stevanović, V. A computational framework for automation of point defect calculations. *Comput. Mater. Sci.* **2017**, *130*, 1−9.
(59) Zhang, S.; Northrup, J. E. Chemical potential dependence of defect formation energies in GaAs: Application to Ga self-diffusion. *Phys. Rev. Lett.* **1991**, *67* (17), 2339.
(60) Arrigoni, M.; Madsen, G. K. Spinney: Post-processing of first-principles calculations of point defects in semiconductors with Python. *Comput. Phys. Commun.* **2021**, *264*, 107946.
(61) Kumagai, Y.; Oba, F. Electrostatics-based finite-size corrections for first-principles point defect calculations. *Phys. Rev. B* **2014**, *89* (19), 195205.
(62) Lyons, J. L.; Van de Walle, C. G. Computationally predicted energies and properties of defects in GaN. *Npj Comput. Mater.* **2017**, *3* (1), 12.
(63) Li, D.; Zhang, A.; Feng, Z.; Wang, W. Theoretical insights on the charge state and bifunctional OER/ORR electrocatalyst activity in 4d-transition-metal-doped g-C3N4 monolayers. *ACS Appl. Mater. Interfaces* **2024**, *16* (5), 5779−5791.
(64) Alkauskas, A.; Yan, Q.; Van de Walle, C. G. First-principles theory of nonradiative carrier capture via multiphonon emission. *Phys. Rev. B* **2014**, *90* (7), 075202.
(65) Darakchieva, V.; Monemar, B.; Usui, A.; Saenger, M.; Schubert, M. Lattice parameters of bulk GaN fabricated by halide vapor phase epitaxy. *J. Cryst. Growth* **2008**, *310* (5), 959−965.
(66) Bhuiyan, A. G.; Hashimoto, A.; Yamamoto, A. Indium nitride (InN): A review on growth, characterization, and properties. *J. Appl. Phys.* **2003**, *94* (5), 2779−2808.
(67) Komsa, H.-P.; Broqvist, P.; Pasquarello, A. Alignment of defect levels and band edges through hybrid functionals: Effect of screening in the exchange term. *Phys. Rev. B* **2010**, *81* (20), 205118.
(68) Dahinden, P.; Broqvist, P.; Pasquarello, A. Charge transition levels of nitrogen dangling bonds at Si/SiO 2 interfaces: A first-principles study. *Phys. Rev. B* **2010**, *81* (8), 085331.
(69) McCluskey, M.; Van de Walle, C.; Romano, L.; Krusor, B.; Johnson, N. Effect of composition on the band gap of strained In x Ga 1− x N alloys. *J. Appl. Phys.* **2003**, *93* (7), 4340−4342.
(70) Siozade, L.; Leymarie, J.; Disseix, P.; Vasson, A.; Mihailovic, M.; Grandjean, N.; Leroux, M.; Massies, J. Modelling of thermally detected optical absorption and luminescence of (In, Ga) N/GaN heterostructures. *Solid State Commun.* **2000**, *115* (11), 575−579.
(71) Wu, J.; Walukiewicz, W.; Yu, K.; Ager, J., III; Li, S.; Haller, E.; Lu, H.; Schaff, W. J. Universal bandgap bowing in group-III nitride alloys. *Solid State Commun.* **2003**, *127* (6), 411−414.
(72) Orsal, G.; El Gmili, Y.; Fressengeas, N.; Streque, J.; Djerboub, R.; Moudakir, T.; Sundaram, S.; Ougazzaden, A.; Salvestrini, J.-P. Bandgap energy bowing parameter of strained and relaxed InGaN layers. *Opt. Mater. Express* **2014**, *4* (5), 1030−1041.
(73) Fadhilah, N.; Wahyuono, R. A.; Rois, M. F.; Risanti, D. D. Resolving two pathways of Al (OH) 3 formation in hydrogen production from aluminum water reaction. *Int. J. Hydrogen Energy* **2025**, *143*, 112−120.
(74) Yue, S.; Li, D.; Zhang, A.; Yan, Y.; Yan, H.; Feng, Z.; Wang, W. Rational design of single transition-metal atoms anchored on a PtSe 2 monolayer as bifunctional OER/ORR electrocatalysts: a defect chemistry and machine learning study. *J. Mater. Chem. A* **2024**, *12* (9), 5451−5463.
(75) Zhang, J.; Liu, Y.; Yang, C.; Qu, Y.; Zhang, A.; Feng, Z.; Wang, W.; Ou, P. Design of bifunctional oxygen evolution/reduction electrocatalysts on g-C3N3 monolayer by a defect physics method. *J. Catal* **2025**, *447*, 116135.
(76) Yao, W.; Qu, Y.; Zhou, M.; Wang, W.; Zhang, A.; Feng, Z.; Yan, H. Increasing the bifunctional OER/ORR activity of 3d transition metals doped g-C3N3 by controlling the charge states. *Mol. Catal* **2024**, *554*, 113807.
(77) Buckeridge, J.; Catlow, C. R. A.; Scanlon, D.; Keal, T.; Sherwood, P.; Miskufova, M.; Walsh, A.; Woodley, S.; Sokol, A. Determination of the nitrogen vacancy as a shallow compensating center in GaN doped with divalent metals. *Phys. Rev. Lett.* **2015**, *114* (1), 016405.
(78) Roccato, N.; Piva, F.; De Santi, C.; Buffolo, M.; Haller, C.; Carlin, J.-F.; Grandjean, N.; Meneghesso, G.; Zanoni, E.; Meneghini, M. Effects of quantum-well indium content on deep defects and reliability of InGaN/GaN light-emitting diodes with under layer. *J. Phys. D: Appl. Phys.* **2021**, *54* (50), 505108.
(79) Armstrong, A. M.; Crawford, M. H.; Koleske, D. D. Contribution of deep-level defects to decreasing radiative efficiency of InGaN/GaN quantum wells with increasing emission wavelength. *Appl. Phys. Express.* **2014**, *7* (3), 032101.
(80) Hammersley, S.; Kappers, M.; Massabuau, F.-P.; Sahonta, S.-L.; Dawson, P.; Oliver, R.; Humphreys, C. Effects of quantum well growth temperature on the recombination efficiency of InGaN/GaN multiple quantum wells that emit in the green and blue spectral regions. *Appl. Phys. Lett.* **2015**, *107* (13), 132106.
(81) Tak, T.; Chow, Y. C.; Nakamura, S.; DenBaars, S. P.; Weisbuch, C.; Speck, J. S. Unexpected origin of the quantum efficiency reduction in long-wavelength (In, Ga) N light-emitting diodes. *Phys. Rev. Appl.* **2025**, *23* (3), 034002.
(82) Dai, Q.; Shan, Q.; Wang, J.; Chhajed, S.; Cho, J.; Schubert, E. F.; Crawford, M. H.; Koleske, D. D.; Kim, M.-H.; Park, Y. Carrier recombination mechanisms and efficiency droop in GaInN/GaN light-emitting diodes. *Appl. Phys. Lett.* **2010**, *97* (13), 133507.
(83) Espenlaub, A. C.; Myers, D. J.; Young, E. C.; Marcinkevičius, S.; Weisbuch, C.; Speck, J. S. Evidence of trap-assisted Auger recombination in low radiative efficiency MBE-grown III-nitride LEDs. *J. Appl. Phys.* **2019**, *126* (18), 184502.
(84) Piprek, J. Efficiency droop in nitride-based light-emitting diodes. *Phys. Status Solidi A* **2010**, *207* (10), 2217−2225.
(85) Dai, Q.; Shan, Q.; Cho, J.; Schubert, E. F.; Crawford, M. H.; Koleske, D. D.; Kim, M.-H.; Park, Y. On the symmetry of efficiency-versus-carrier-concentration curves in GaInN/GaN light-emitting diodes and relation to droop-causing mechanisms. *Appl. Phys. Lett.* **2011**, *98* (3), 033506.
(86) Olivier, F.; Daami, A.; Licitra, C.; Templier, F. Shockley-Read-Hall and Auger non-radiative recombination in GaN based LEDs: A size effect study. *Appl. Phys. Lett.* **2017**, *111* (2), 022104.
(87) Shen, Y.; Mueller, G.; Watanabe, S.; Gardner, N.; Munkholm, A.; Krames, M. Auger recombination in InGaN measured by photoluminescence. *Appl. Phys. Lett.* **2007**, *91* (14), 141101.

https://doi.org/10.1021/acsanm.6c01138
ACS Appl. Nano Mater. 2026, 9, 9478−9486